Numerical Investigation of Turbulent Flow over a Randomly Packed Sediment Bed Using a Variable Porosity Continuum Model

Shashank K. Karra[1, a)] and Sourabh V. Apte[1, b)]

School of Mechanical, Industrial and Manufacturing Engineering,

Oregon State University, Corvallis, OR, 97331

(Dated: 28 May 2025)

A large eddy simulation (LES) is performed for a turbulent open channel flow over a porous sediment bed at permeability Reynolds number of $Re_K \sim 2.56$ (Re_τ=270) representative of aquatic systems. A continuum approach based on the upscaled, volume-averaged Navier-Stokes (VaNS) equations is used by defining smoothly varying porosity across the sediment water interface (SWI) and modeling the drag force in the porous bed using a modified Ergun equation with Forchheimer corrections for inertial terms. The results from the continuum approach are compared with a pore-resolved direct numerical simulation (PR-DNS) in which turbulent flow over a randomly packed sediment bed of monodispersed particles is investigated as in Karra *et al.*[1]. A spatially varying porosity profile generated from the pore-resolved DNS is used in the continuum approach. Mean flow, Reynolds stress statistics, and net momentum exchange between the freestream and the porous bed are compared between the two studies, showing reasonably good agreement. Small deviations within the transitional region between the sediment bed and the freestream as compared to the PR-DNS results are attributed to the local protrusions of particles in a randomly packed bed that are absent in the continuum approach, but are present in the PR-DNS. A better representation of the effective permeability in the top transition layer that accounts for roughness effect of exposed particles is necessary. The continuum approach significantly reduces the computational cost, thereby making it suitable to study hyporheic exchange of mass and momentum in large scale aquatic domains with combined influence of bedform and bed roughness.

[a)]karras@oregonstate.edu

[b)]sourabh.apte@oregonstate.edu; `https://web.engr.oregonstate.edu/~sva/apte.html`

I. INTRODUCTION

Large scale turbulent flows over permeable beds and structures are commonly encountered in a wide range of problems; for example, flows in a long oil wellbore which are surrounded by a porous formation, stream or river flows over porous sediment beds, and atmospheric flows over plant canopies and densely built-up urban areas which can be modeled as a permeable domain. Of importance is the hyporheic transient storage or retention and transport of solutes such as chemicals and pollutants, dissolved oxygen, nutrients, and heat from the streamflow to the ground water across the sediment-water interface (SWI) in stream or river flows. This hyporheic transient storage is one of the most important concepts for stream ecology, and has enormous societal value in predicting source of fresh drinking water, transport, biogeochemical processing of nutrients, and sustaining diverse aquatic ecosystems[2–8].

A broad range of spatio-temporal scales corresponding to disparate physical and chemical processes contribute to the mixing within the hyporheic zone. Turbulent transport across the SWI, coherent flow structures, and non-Darcy flow within the sediment bed have been hypothesized as critical mechanisms impacting transient storage. The importance of penetration of turbulence within the bed and near bed pressure fluctuations are crucial and their impact on the hyporheic transient storage is poorly understood[9]. While there are many parameters which characterize exchange of mass and momentum across the sediment water interface (SWI), the permeability Reynolds number, representing the ratio between the permeability scale to the viscous scale $Re_K = \sqrt{K}/(\nu/u_\tau)$, is typically used to identify different flow regimes based on the dominant transport mechanisms across the SWI. Here, u_τ is the friction velocity, K is the bed permeability, and ν is the kinematic viscosity. Based on the characterization developed by Grant, Gomez-Velez, and Ghisalberti[8], Voermans, Ghisalberti, and Ivey[10], turbulence is dominant near the SWI and can penetrate few layers of the sediment bed for $Re_K > 1$. Bed permeability was found to increase friction coefficient, reduce the wall-blocking effect due to impermeable rough walls, reduce near-bed anisotropy in turbulence intensities, and influence flow resistance dramatically Manes *et al.*[11].

Recently, there have been few fundamental experimental investigations of turbulent flow over a mono-dispersed sediment bed using refractive-index matched particle tracking velocimetry over a wide range of $Re_K = 0.36$–6.3 and showed that for $Re_K = \mathcal{O}(1-10)$, the

turbulence shear penetration depth, a measure of true roughness felt by the flow, normalized by the permeability scale ($\sqrt{K}$) is a non-linear function of Re_K. Kim *et al.*[12] also investigated, through experimental observations at $Re_K = 50$, the dynamic interplay between surface and subsurface flow in the presence of smooth and rough permeable walls, composed of a uniform cubic arrangement of packed spheres. They confirmed the existence of amplitude modulation, a phenomenon typically identified in impermeable boundaries, whereby the outer large scales modulate the intensity of the near-wall small scale turbulence. However, detailed data on the pressure field at the SWI is lacking.

Pore-resolved direct numerical simulations (PR-DNS) has recently been used to study turbulent stream flow over the hyporheic zone, wherein the smallest scales of geometrical features such as pore size or the diameter of solid particles in the porous medium as well the smallest scales of flow turbulence observed in the free-stream region close to the permeable bed are fully resolved. The accuracy associated with PR-DNS, however, comes at an enormous computational cost. Karra *et al.*[1] pushed the limits of such detailed simulations for flow over a randomly packed bed over a range of Re_K up to 9, to obtain detailed data on pressure variations and drag forces on the sediment grains. However, conducting such simulations at even larger and practical scale Reynolds numbers is still out of reach even for the most powerful supercomputers today.

Reduced-order *homogenized* modeling approaches based on upscaled and averaged governing equations, requiring less computational resources, are necessary and have been used to simulate flow over permeable beds and walls. Method of volume averaging was developed and applied by Whitaker[13] to obtain a continuum model for the superficial velocity through the porous bed. In this approach, the averaged equations are derived by applying volume averaging over a representative filter volume to the continuity, momentum, and energy equations. Similar to the volume filtered equations in large-eddy simulation (LES) approach, the volume-averaged Navier-Stokes (VaNS) equations require closure models for sub-filter scale stresses and forces on the surfaces of solid grains in the bed.

The method of volume averaging usually splits the domain into freestream with porosity ($\phi = 1$) and porous region with spacial variation of porosity. The boundary between the porous region and the freestream in a typical *two-domain approach* is treated by ensuring continuity of flow variables while prescribing a stress jump condition at the interface[14–16] with coefficients calibrated using experimental data. Beavers and Joseph[17] incorporated the

effect of bed permeability through slip boundary conditions at the interface of a permeable bed and a laminar channel flow, wherein porous flow in the bed is governed by Darcy's law. Saffman [18] through their theoretical work showed that the interface boundary condition is valid with an assumption of Stokes flow near the interface and inside the permeable bed. Therefore, the interface condition proposed by Beavers and Joseph [17] can only be applied to turbulent channel flow when a viscous sublayer exits close to the permeable wall. Hahn, Je, and Choi [19] performed DNS of turbulent flow in channel bounded by a permeable wall, by extending this interface boundary condition, and showed that the requirement of a viscous sublayer adjacent to the permeable bed is met when bed permeability length scale, $\sqrt{K}$, is smaller compared to the viscous length scale ν/u_τ. Therefore, for small values of Re_K, which is a ratio of both these scales, turbulent eddies are blocked by the wall and consequently a viscous sublayer exits. However, at larger values of Re_K the eddies penetrate into the bed prohibiting the formation of the viscous sublayer. At Re_K numbers representative of aquatic flows, there is a critical need to model the flow inside the permeable bed as a continuum, coupled with free-stream flow. Recently, Rosti, Cortelezzi, and Quadrio [16] have used DNS to study turbulent channel flow over porous beds, where the flow in channel region was described by Navier-Stokes equations, while VaNS equations were solved in the very low permeability bed, and two sets of equations were coupled at the interface between fluid and porous material via a momentum-transfer coefficient. The mean particle size was small, which meant that the flow was not in the fully rough wall regime.

For randomly packed bed of particles, defining an interface between the free-stream and porous region in the two-domain approach is not straightforward owing to local protrusions and roughness elements of the top layer of particles in the bed. An alternative *single-domain* approach wherein the porous region is considered as a pseudo-fluid and the composite region is treated as a continuum with smooth variation of the porosity and permeability across the two regions[20–23]. Application of such a single-domain, variable porosity (or permeability) model for turbulent flows requires disparate filtering volumes for the freestream region and the porous region. To capture the rapid bed-normal variations in the fluid flow variables in the turbulent freestream, a filter based on the computational grid with thin bed-parallel volumes is needed. On the other hand, the representative averaging volume within the porous bed is typically much larger[24]. Breugem and Boersma [23] addressed this scale mismatch by applying a very gradual change in the averaging volume near the interface to study turbulent

flow over porous medium consisting of uniformly arranged particles. A fifth-order porosity variation in the bed-normal direction to smoothly transition between between the porous and freestream regions. Accordingly, the explicit information on the spatial filter is hidden in the model for the drag force and the subfilter-scale stresses, and they used DNS-like very fine resolution in the bed-normal direction. Pokrajac and De Lemos[24] developed the volume averaging equations by allowing the filtering volume to vary in space, especially in the bed-normal direction. With spatially varying averaging volumes, derivative of an averaged quantity and average of a derivative do not commute resulting in additional terms. Recently, Sadowski *et al.*[25] evaluated these commutation errors for same turbulent flow over a porous channel as investigated by Breugem and Boersma[23] and showed that they are important in the transition region, however, their magnitude was much smaller than the drag force especially if a fine mesh is used in the transition region. These studies involved highly porous beds with artificial arranged packing and bed porosity in the homogeneous region ranging over 0.6–0.95. In addition, the friction Reynolds number was small and not in the hydrodynamically rough regime typical of aquatic flows.

In this work, the predictive capability of variable porosity, single domain approach is evaluated for the turbulent flow over a monodispersed, randomly arranged in a close-packed sediment bed in the hydrodynamically rough regime corresponding to our prior PR-DNS study Karra *et al.*[1]. The single domain approach is chosen over the two-domain approach to avoid complexities related to specifying a jump condition in stress, which needs modeling and the coefficients involved are not known a priori. In addition, it is unclear on how to model subfilter scale stresses with the two-domain approach. The variable porosity approach similar to Breugem and Boersma[23] is used by matching the bed-normal variation of the porosity to the porosity distribution obtained from the randomly arranged particle layers. The drag force within the bed is modeled using the modified Ergun equation with Forchheimer corrections for the inertial terms. To the best of authors' knowledge, this is one of the first studies where the single-domain variable porosity approach has been used for turbulent flows in the fully rough wall regime.

The paper is arranged as follows. The volume-averaged continuum equations and the related closure model are described in section II. The numerical approach for the diffuse interface model is briefly discussed in section III. The flow domain, simulation parameters, and grid resolution are also described in section III. Details of the validation study, mean

flow and Reynolds stress statistics, net momentum exchange between the free-stream and the porous bed, pressure fluctuations, and turbulent kinetic energy budgets are compared in section IV. Finally, section V summarizes the results.

II. MATHEMATICAL FORMULATION

In this section the continuum approach based on the volume-averaged Navier Stokes equations (Whitaker [13]) for flows in porous media is briefly discussed.

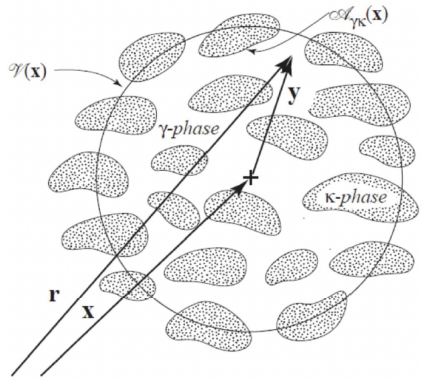

FIG. 1. Schematic of the averaging volume over the solid (κ) and the fluid (γ) phase in a porous medium[13].

Figure 1 shows a schematic of a representative elementary volume (REV) over which averaging is performed to derive the volume-averaged Navier-Stokes (VaNS) equations. Here, γ represents the fluid phase, κ represents the solid phase, $\mathscr{A}_{\gamma\kappa}(\mathbf{x})$ represents the surface area between the κ and γ-phases, and $\mathscr{V}(\mathbf{x})$ is the averaging domain encompassing the fluid and solid phases where $\mathbf{x}$ is its centroid. To obtain meaningful VaNS equations, it is assumed that the equivalent length scale associated with the pore size is much smaller than the length scale associated with the REV, which in turn is much smaller than the global length scale of the porous medium. In addition, variations in porosity averaged over the REV are typically negligible. However, porosity will vary across the sediment water interface (SWI) in flow over a porous sediment. The volume averaging operator is represented as $\langle\cdot\rangle$ and when applied to any quantity ψ in the fluid (γ) phase gives,

$$\langle\psi_\gamma\rangle = \frac{1}{\mathscr{V}}\int_{\mathbf{r}\in\mathscr{V}(\mathbf{X})} I_\gamma(\mathbf{r})\psi(\mathbf{r})d\mathscr{V}(\mathbf{r}), \tag{1}$$

where $\mathscr{V}$ is the total volume in the averaging domain and $I_\gamma(\mathbf{r})$ is the indicator function

defined as

$$I_\gamma(\mathbf{r}) = \begin{cases} 1, & \mathbf{r} \in \mathscr{V}_\gamma, \\ 0, & \mathbf{r} \in \mathscr{V}_\kappa. \end{cases} \tag{2}$$

It can be observed that the volume averaging operator acts as a spatial filter only capturing the resolved-scale structure of the flow field.

The intrinsic average is defined in a similar fashion except that the averaging volume used is the volume of the fluid phase,

$$\langle \psi_\gamma \rangle^\gamma = \frac{1}{\mathscr{V}_\gamma} \int_{\mathbf{r} \in \mathscr{V}(\mathbf{X})} I_\gamma(\mathbf{r}) \psi(\mathbf{r}) d\mathscr{V}(\mathbf{r}). \tag{3}$$

As a result, the superficial averaged quantity $\langle \psi_\gamma \rangle$ can be related with the intrinsic averaged quantity $\langle \psi_\gamma \rangle^\gamma$ as

$$\langle \psi_\gamma \rangle = \varepsilon_\gamma \langle \psi_\gamma \rangle^\gamma, \tag{4}$$

where ε_γ is the porosity of the medium, defined as the ratio of the void volume to the total volume and obtained from equation 1 with $\psi(\mathbf{r}) = 1$.

In addition, Whitaker[13] used the spatial averaging theorem assuming that the *averaging volume does not change* and provided a relationship between the volume-averaged spatial derivative and the spatial derivative of the volume-averaged quantity as

$$\langle \nabla \psi_\gamma(\mathbf{r}) \rangle = \nabla \langle \psi_\gamma \rangle + \frac{1}{\mathscr{V}_\gamma} \int_{\mathbf{r} \in \mathscr{A}_{\gamma\kappa}(\mathbf{X})} \mathbf{n}_{\gamma\kappa}(\mathbf{r}) \psi_\gamma(\mathbf{r}) d\mathscr{A}(\mathbf{r}), \tag{5}$$

where $\mathbf{n}_{\gamma\kappa}$ is the unit normal vector pointing from κ phase to the γ phase. The volume averaging procedure can be applied to the continuity and momentum equations for an incompressible fluid, using $\widetilde{\boldsymbol{u}}_\gamma$ and $\widetilde{p}_\gamma$ as the spatial fluctuations in velocity and pressure, defined as

$$\widetilde{\boldsymbol{u}}_\gamma = \boldsymbol{u}_\gamma - \langle \boldsymbol{u}_\gamma \rangle^\gamma, \quad \widetilde{p}_\gamma = p_\gamma - \langle p_\gamma \rangle^\gamma. \tag{6}$$

With this method, the volume-averaged continuum equations for stationary porous medium with spatial variations in porosities are obtained as[13,26]

$$\nabla \cdot (\varepsilon_\gamma \langle \boldsymbol{u}_\gamma \rangle^\gamma) = 0, \tag{7}$$

$$\rho_\gamma \frac{\partial \varepsilon_\gamma \langle \boldsymbol{u}_\gamma \rangle^\gamma}{\partial t} + \underbrace{\rho_\gamma \nabla \cdot \langle \boldsymbol{u}_\gamma \otimes \boldsymbol{u}_\gamma \rangle}_{\text{volume filter closure}} = -\varepsilon_\gamma \nabla \langle p_\gamma \rangle^\gamma + \mu_\gamma \varepsilon_\gamma \nabla^2 \langle \boldsymbol{u}_\gamma \rangle^\gamma + \mu_\gamma \nabla \varepsilon_\gamma \cdot \nabla \otimes \langle \boldsymbol{u}_\gamma \rangle^\gamma + \mu_\gamma \langle \boldsymbol{u}_\gamma \rangle^\gamma \nabla^2 \varepsilon_\gamma + \underbrace{\frac{1}{\mathscr{V}} \int_{\mathscr{A}_{\gamma\kappa}} \mathbf{n}_{\gamma\kappa} \cdot (-\mathbf{I}\widetilde{p}_\gamma + \mu_\gamma \nabla \otimes \widetilde{\mathbf{u}}_\gamma) \mathbf{d}\mathscr{A}}_{\text{surface filter closure}} + \rho_\gamma \varepsilon_\gamma \mathbf{f_b}. \tag{8}$$

Here ρ_γ is the fluid density, μ_γ is the dynamic viscosity, and $\mathbf{f_b}$ is the body force per unit mass due to gravity or external pressure gradient. Because of the non-linear inertial terms and volume averaging across the fluid-solid boundary, two unclosed terms identified as the volume filter closure and surface filter closure are obtained that need to be modeled. The nonlinear product of velocities in the volume filter term can be expanded using volume averaging and spatial deviation and will result in a closure problem involving the subfilter scale stress, which is similar to the subgrid-scale stress in large-eddy simulation (LES). The surface-filter closure term represents the net drag force on the interfacial area $\mathscr{A}_{\gamma\kappa}$ between the γ and κ phases within the averaging volume and also needs to be modeled. The right-hand side of equation 8 has been analyzed[13,26]. The viscous terms on the right hand side of equation 8 represent the Brinkman correction terms.

A. Volume Filter Closure

The nonlinear advective term can be written as,

$$\langle \mathbf{u}_\gamma \otimes \mathbf{u}_\gamma \rangle = \langle \langle \mathbf{u}_\gamma \rangle^\gamma \otimes \langle \mathbf{u}_\gamma \rangle^\gamma \rangle + \langle \langle \mathbf{u}_\gamma \rangle^\gamma \otimes \widetilde{\mathbf{u}}_\gamma \rangle + \langle \widetilde{\mathbf{u}}_\gamma \otimes \langle \mathbf{u}_\gamma \rangle^\gamma \rangle + \langle \widetilde{\mathbf{u}}_\gamma \otimes \widetilde{\mathbf{u}}_\gamma \rangle \tag{9}$$

$$\approx \langle 1 \rangle \langle \mathbf{u}_\gamma \rangle^\gamma \otimes \langle \mathbf{u}_\gamma \rangle^\gamma + \langle \mathbf{u}_\gamma \rangle^\gamma \otimes \langle \widetilde{\mathbf{u}}_\gamma \rangle + \langle \widetilde{\mathbf{u}}_\gamma \rangle \otimes \langle \mathbf{u}_\gamma \rangle^\gamma + \langle \widetilde{\mathbf{u}}_\gamma \otimes \widetilde{\mathbf{u}}_\gamma \rangle, \tag{10}$$

where the above approximation assumes that the interstitial volume of the fluid γ-phase is much smaller than the averaging volume[26]. Under these conditions $\langle \widetilde{\mathbf{u}}_\gamma \rangle = 0$ and the above term simplifies to,

$$\langle \mathbf{u}_\gamma \otimes \mathbf{u}_\gamma \rangle \approx \varepsilon_\gamma \langle \mathbf{u}_\gamma \rangle^\gamma \otimes \langle \mathbf{u}_\gamma \rangle^\gamma + \langle \widetilde{\mathbf{u}}_\gamma \otimes \widetilde{\mathbf{u}}_\gamma \rangle \equiv \varepsilon_\gamma \langle \mathbf{u}_\gamma \rangle^\gamma \otimes \langle \mathbf{u}_\gamma \rangle^\gamma + \varepsilon_\gamma \langle \widetilde{\mathbf{u}}_\gamma \otimes \widetilde{\mathbf{u}}_\gamma \rangle, \tag{11}$$

where $\langle 1 \rangle = \varepsilon_\gamma$ is used, and the second term is represented in terms of the intrinsic average. The first term is essentially the advective term and is closed in terms of the intrinsic velocity $\langle \mathbf{u} \rangle^\gamma$. The second-term represents the subfilter-scale stress and is very similar to the subgrid-

scale stress in the freestream, where $\varepsilon_\gamma = 1$. Substituting equation (11) into equation (8), the volume filtered momentum equation can be rewritten as,

$$\begin{aligned}\rho_\gamma \frac{\partial \varepsilon_\gamma \langle \boldsymbol{u}_\gamma \rangle^\gamma}{\partial t} + \rho_\gamma \nabla \cdot \left[\varepsilon_\gamma \langle \boldsymbol{u}_\gamma^\gamma \rangle \otimes \langle \boldsymbol{u}_\gamma^\gamma \rangle\right] + \underbrace{\rho_\gamma \nabla \cdot \left[\varepsilon_\gamma \langle \widetilde{\mathbf{u}}_\gamma \otimes \widetilde{\mathbf{u}}_\gamma \rangle\right]}_{\text{volume filter closure}} = -\varepsilon_\gamma \nabla \langle p_\gamma \rangle^\gamma + \\ \left[\underline{\mu_\gamma \varepsilon_\gamma \nabla^2 \langle \boldsymbol{u}_\gamma \rangle^\gamma} + \underline{\mu_\gamma \nabla \varepsilon_\gamma \cdot \nabla \otimes \langle \boldsymbol{u}_\gamma \rangle^\gamma} + \mu_\gamma \langle \boldsymbol{u}_\gamma \rangle^\gamma \nabla^2 \varepsilon_\gamma\right] + \\ \underbrace{\frac{1}{\mathscr{V}} \int_{\mathscr{A}_{\gamma\kappa}} \mathbf{n}_{\gamma\kappa} \cdot (-\mathbf{I}\widetilde{p}_\gamma + \mu_\gamma \nabla \otimes \widetilde{\mathbf{u}}_\gamma) \mathbf{d}\mathscr{A}}_{\text{surface filter closure}} + \rho_\gamma \varepsilon_\gamma \mathbf{f_b}.\end{aligned} \tag{12}$$

Combining the first two viscous terms on the right hand side of the above equation and rearranging the momentum equation simplifies to,

$$\begin{aligned}\rho_\gamma \frac{\partial \varepsilon_\gamma \langle \boldsymbol{u}_\gamma \rangle^\gamma}{\partial t} + \rho_\gamma \nabla \cdot \left[\varepsilon_\gamma \langle \boldsymbol{u}_\gamma^\gamma \rangle \otimes \langle \boldsymbol{u}_\gamma^\gamma \rangle\right] = -\varepsilon_\gamma \nabla \langle p_\gamma \rangle^\gamma + \mu_\gamma \nabla \cdot \left[\varepsilon_\gamma \nabla \otimes \langle \boldsymbol{u}_\gamma \rangle^\gamma\right] + \mu_\gamma \langle \boldsymbol{u}_\gamma \rangle^\gamma \nabla^2 \varepsilon_\gamma + \\ \underbrace{\frac{1}{\mathscr{V}} \int_{\mathscr{A}_{\gamma\kappa}} \mathbf{n}_{\gamma\kappa} \cdot (-\mathbf{I}\widetilde{p}_\gamma + \mu_\gamma \nabla \otimes \widetilde{\mathbf{u}}_\gamma) \mathbf{d}\mathscr{A}}_{\text{surface filter closure}} - \underbrace{\rho_\gamma \nabla \cdot \left[\varepsilon_\gamma \langle \widetilde{\mathbf{u}}_\gamma \otimes \widetilde{\mathbf{u}}_\gamma \rangle\right]}_{\text{volume filter closure}} + \rho_\gamma \varepsilon_\gamma \mathbf{f_b}.\end{aligned} \tag{13}$$

Closures for this subfilter stress in the porous region are needed and algebraic models have been proposed[27]. For the streamflow, this term can be modeled using the standard gradient-diffusion hypothesis based on dynamic subgrid scale model[28], typically employed in large-eddy simulation (LES). In the close-pack sediment bed with low porosity, the turbulence fluctuations decay rapidly and are not significant beyond the first top layer of particles as shown by Karra *et al.*[1] in their particle-resolved simulations. Also, as discussed in section III B much finer grid resolutions are used in the present work compared to typical LES resolutions (this is done to minimize grid-based errors and thus any deviations compared to PR-DNS case may be attributed to the VaNS-LES model). Thus, the magnitude of subfilter scale stresses within the homogeneous porous region and in the interface region are small compared to the drag force. To allow seamless application of the dynamic subgrid scale model in the freestream and the transitional region, the dynamic subgrid scale model is used throughout the domain with subgrid-scale viscosity (μ_{sgs}) obtained using porosity-weighted intrinsic velocity similar to the Favre-averaging procedure typically employed in variable density flows. The momentum equation with subgrid eddy viscosity model for the

volume filter closure term becomes,

$$\rho_\gamma \frac{\partial \varepsilon_\gamma \langle \boldsymbol{u}_\gamma \rangle^\gamma}{\partial t} + \rho_\gamma \nabla \cdot \left[\varepsilon_\gamma \langle \boldsymbol{u}_\gamma^\gamma \rangle \otimes \langle \boldsymbol{u}_\gamma^\gamma \rangle \right] = -\varepsilon_\gamma \nabla \langle p_\gamma \rangle^\gamma + \nabla \cdot \left[\left(\mu_\gamma + \mu_{\text{sgs}} \right) \varepsilon_\gamma \nabla \otimes \langle \boldsymbol{u}_\gamma \rangle^\gamma \right] + \mu_\gamma \langle \boldsymbol{u}_\gamma \rangle^\gamma \nabla^2 \varepsilon_\gamma + \underbrace{\frac{1}{\mathscr{V}} \int_{\mathscr{A}_{\gamma\kappa}} \mathbf{n}_{\gamma\kappa} \cdot (-\mathbf{I}\widetilde{p}_\gamma + \mu_\gamma \nabla \otimes \widetilde{\mathbf{u}}_\gamma) \mathbf{d}\mathscr{A}}_{\text{surface filter closure}} + \rho_\gamma \varepsilon_\gamma \mathbf{f}_\mathbf{b}. \quad (14)$$

Similar to the open-channel flows, the constant in subgrid viscosity is obtained by averaging in the homogeneous directions (x-z plane). Breugem, Boersma, and Uittenbogaard [29] used scaling arguments to show that this term is negligible in the homogeneous porous region as well as the the transitional region between the porous bed and streamflow. In addition, they used highly refined mesh in the freestream to accurately capture the subgrid scales, and thus neglected this term throughout the domain.

B. Surface Filter Closure

As shown by Whitaker [13], Ochoa-Tapia and Whitaker [14] using theoretical analysis, the surface filter term can be expressed in terms of an effective permeability,

$$\frac{1}{\mathscr{V}} \int_{\mathscr{A}_{\gamma\kappa}} \mathbf{n}_{\gamma\kappa} \cdot (-\mathbf{I}\widetilde{p}_\gamma + \mu_\gamma \nabla \otimes \widetilde{\mathbf{u}}_\gamma) \mathbf{d}\mathscr{A} = -\mu_\gamma \varepsilon_\gamma \mathbf{K}_{\text{eff}}^{-1} \left[\varepsilon_\gamma \langle \boldsymbol{u}_\gamma \rangle^\gamma \right] = -\mu_\gamma \varepsilon_\gamma \mathbf{K}_{\text{eff}}^{-1} \langle \boldsymbol{u}_\gamma \rangle, \quad (15)$$

where $\mathbf{K}_{\text{eff}}$ is the effective permeability tensor and $\langle \boldsymbol{u}_\gamma \rangle$ is the superficial velocity. The effective permeability tensor is generally expressed as

$$\mathbf{K}_{\text{eff}}^{-1} = \mathbf{K}^{-1} \left(\mathbf{I} + \mathbf{F} \right), \quad (16)$$

where $\mathbf{K}$ and $\mathbf{F}$ are the permeability and Forchheimer tensors, respectively.

In the limit of Stokes flow, the drag term depends only on the permeability tensor, whereas the inertial effects are important at higher pore Reynolds numbers such that the Forchheimer correction becomes dominant. The permeability tensor depends only on the geometry of the porous medium, but the Forchheimer tensor can depend on the pore Reynolds number, the orientation of the beads relative to the direction of the volume-averaged flow and pressure gradient, as well as other geometric parameters. Universally valid expressions for these tensors have not been successfully developed. They are determined empirically

through substantial experimental data and numerical simulations in the Stokes and steady or unsteady laminar regimes. For flow fields through packed sediment beds, as modeled in this work, a widely used relation for the drag force is the Ergun equation, which can be written using the permeability and Forchheimer tensors as

$$\mathbf{K} = \frac{d_p^2 \varepsilon_\gamma^3}{A(1-\varepsilon_\gamma)^2}\mathbf{I}, \quad \mathbf{F} = \frac{\varepsilon_\gamma}{B(1-\varepsilon_\gamma)}\frac{\rho_\gamma d_p |\langle \boldsymbol{u}_\gamma \rangle^\gamma|}{\mu_\gamma}\mathbf{I}, \tag{17}$$

where $d_p = 6\mathscr{V}_\kappa/\mathscr{A}_{\gamma\kappa}$ is the effective diameter of the solid beads with $\mathscr{V}_\kappa$ their volume and $\mathscr{A}_{\kappa\gamma}$ the surface area. Several different values have been proposed for the model coefficients A and B[29–32]. Bağcı, Dukhan, and Özdemir[32] obtained experimental data on a wide range of Reynolds numbers with steel spheres of two different diameters and fitted the data with $A = 150$ and $A/B = 1.0$–1.75. Macdonald *et al.*[31] used experimental and computational data in which particle sizes, porosity, and pore Reynolds numbers were varied and proposed using $A = 180$ and $A/B = 1.8$–4 as well as replacing ε_γ^3 by $\varepsilon_\gamma^{3.6}$. In the present study the coefficient A is adjusted to match the pore-resolved permeability deep within the bed obtained from the PR-DNS data, whereas the coefficient for the Forchheimer correction is set to $B = 100$, which is a standard value used in these models, (e.g Breugem *et al.*[29]). Note that the Forchheimer correction does change based on the local intrinsic velocity or Reynolds numbers. Also, the Forchheimer correction is only be present in the top layer of the sediment (in the interface region) since the intrinsic velocity decays rapidly reaching Darcy velocity deep inside the bed, where the Forchheimer correction has negligible effect.

The viscous term involving $\nabla^2\varepsilon_\gamma$ is important when the porosity varies spatially, for example in the sediment-water interface region. For such variable porosity case, no simple representation of the area integral is available. This transitional region can be represented by momentum jump conditions[14]; however, this results in the two-domain formulation with jump conditions specified as interface conditions between the two domains. In the present work, a single-domain, variable porosity approach is used similar to the work of Breugem and Boersma[23], Breugem, Boersma, and Uittenbogaard[29]. The drag force in the transition region between the porous bed and the streamflow is assumed to be represented by the above permeability and Forchheimer tensors that depend on the local porosity variations. The effectiveness of this assumption is evaluated in the present work for a randomly packed, sediment bed.

III. NUMERICAL APPROACH AND SIMULATION SETUP

With a model for effective permeability, the set of equations 7 and 8 can be rewritten for the *intrinsic* velocity ($\langle \mathbf{u}_\gamma \rangle^\gamma$) and pressure ($\langle p_\gamma \rangle^\gamma$) as primitive variables,

$$\nabla \cdot [\varepsilon_\gamma \langle \boldsymbol{u}_\gamma \rangle^\gamma] = 0, \tag{18}$$

$$\begin{aligned} \rho_\gamma \frac{\partial [\varepsilon_\gamma \langle \boldsymbol{u}_\gamma \rangle^\gamma]}{\partial t} + \rho_\gamma \nabla \cdot [\varepsilon_\gamma \langle \boldsymbol{u}_\gamma \rangle^\gamma \langle \boldsymbol{u}_\gamma \rangle^\gamma] = & -\varepsilon_\gamma \nabla \langle p_\gamma \rangle^\gamma + \underbrace{\mu_\gamma \nabla \cdot [\varepsilon_\gamma \nabla \otimes \langle \boldsymbol{u}_\gamma \rangle^\gamma]}_{I} + \\ & \underbrace{\mu_\gamma \nabla^2 \varepsilon_\gamma \langle \boldsymbol{u}_\gamma \rangle^\gamma}_{\mathbf{II}} - \underbrace{\mu_\gamma \mathbf{K}_{\text{eff}}^{-1} \varepsilon_\gamma^2 \langle \boldsymbol{u}_\gamma \rangle^\gamma}_{\mathbf{III}} + \rho_\gamma \varepsilon_\gamma \mathbf{f_b}. \end{aligned} \tag{19}$$

In the freestream region, $\varepsilon_\gamma = 1$ and $\mathbf{K}_{\text{eff}}^{-1} = 0$, and terms **I**, **II**, and **III** drop out resulting in the standard volume-filtered LES equations. In the homogeneous porous bed, $\varepsilon_\gamma = \varepsilon_c$, and the additional viscous term due to porosity variation (**II** drops out, but the effective permeability based drag term remains. In the transitional interface region, ε_γ varies in the bed-normal direction, and thus all terms remain. Terms involving porosity gradients can be significant and comparable to 10-20% of the drag force terms in the transition region.

The numerical approach is based on Cartesian, rectilinear grids with smooth variation in grid resolution across the SWI. A fully parallel, structured, collocated grid, fractional time-stepping based finite volume solver has been developed and used for these simulations. All terms including the viscous terms (**I** and **II**) and the drag force term (**III**) in equation 19 are treated implicitly using the Crank-Nicholson scheme. The implicit treatment of these terms in the porous regime provides significant robustness and avoids very small computational time steps especially for the case with small effective permeability. This allows use of time-steps based on CFL numbers of 0.5. Note that the intrinsic velocity ($\langle \mathbf{u}_\gamma \rangle^\gamma$) is not divergence free. A biconjugate gradient (BiCGStab) solver is used for the pressure Poisson equation to enforce the continuity equation.

A. Simulation domain and parameters

Turbulent flow over a permeable bed, made of monodispersed spherical particles, can be characterized by the permeability Reynolds number ($Re_K = u_\tau \sqrt{K}/\nu$), the friction or turbulent Reynolds number ($Re_\tau = u_\tau \delta/\nu$), the roughness Reynolds number $D^+ = D_p u_\tau/\nu$,

the bulk Reynolds number ($Re_b = \delta U_b/\nu$) the ratio of sediment depth to the free-stream height (H_s/δ), the ratio of the sediment grain diameter to the free-stream height (D_p/δ), bed porosity (ε_γ), type of particle packing (random versus arranged), and the domain lengths in the streamwise and spanwise directions normalized by the free-stream height (L_x/δ, L_z/δ). Here u_τ is the friction velocity, U_b is the bulk velocity, K is the bed permeability and ν is the kinematic viscosity. For monodispersed, spherical particles, the of size of the roughness element, k_s, scales with the permeability ($k_s/\sqrt{K} \approx 9$)[10,33].

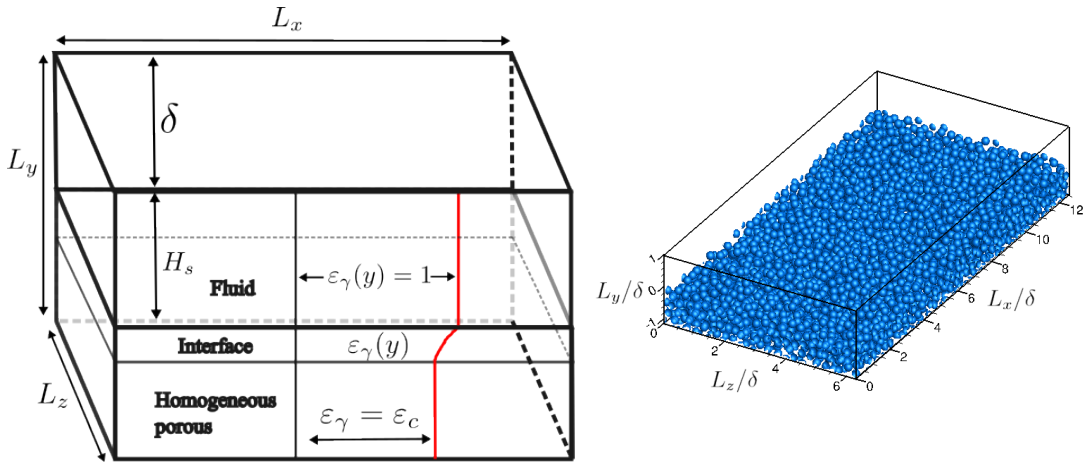

(a) VaNS Domain (b) Sediment Bed

FIG. 2. Schematic disgram for the computational model: (a) domain for the LES-VaNS model, and (b) and the actual sediment bed used in the PR-DNS study[34].

Figure 2a shows the schematic of the sediment bed and the computational domain used in the present study. Also shown is the randomly arrange sediment particle bed (figure 2b) used in the the PR-DNS study[1] which involved a doubly periodic domain (*periodic in streamwise and spanwise directions*) with four layers of randomly packed, monodispersed sediment grains at the bottom to capture the turbulence penetration and unsteady, inertial flow. Same dimensions computational domain is used in the present VaNS-LES computation.

Table I shows detailed simulation parameters for both PR-DNS and VaNS-LES cases. First, a verification and validation (VV) case was simulated for bed porosity $\varepsilon_c = 0.418$, $Re_K \sim 2.65$ and $Re_\tau \sim 186$ using the VaNS-LES approach to directly compare with the experimental data of Voermans, Ghisalberti, and Ivey[10] as well as PR-DNS data from the prior work by authors[1]. Next, keeping the same bed porosity and approximately same $Re_K = 2.56$, the channel free stream height was increased to $3.5D_p$ resulting in friction Reynolds number of $Re_\tau \sim 270$ and simulated using the PR-DNS as well as VaNS-LES

TABLE I. Parameters used in present direct numerical simulations where, D_p is the sphere diameter, δ is the free-stream height, H_s is the sediment depth, and ε is the porosity. L_x and L_z are the streamwise and spanwise domain lengths, Re_K, Re_τ, Re_b and D^+ are the permeability, friction, bulk and roughness Reynolds numbers, respectively. $(\,)^+$ denotes wall units.

Case	Domain	Re_K	Re_τ	Re_b	D^+	ε_γ	H_s/δ	D_p/δ	$(L_x, L_z)/\delta$	$(\Delta x^+, \Delta y^+, \Delta z^+)$
VV	permeable	2.65	186	1,860	80	0.418	1.71	0.43	$(4\pi,2\pi)$	(9.7, 0.95, 6.0)
PR-DNS	permeable	2.56	270	2,826	77	0.418	1.14	0.29	$(4\pi,2\pi)$	(2.94, 0.95, 2.94)
VaNS-LES	permeable	2.5	263	2,829	75	0.418	1.14	0.29	$(4\pi,2\pi)$	(7.5, 0.95, 6.0)
SW-DNS	impermeable	-	270	4,461	0	-	-	-	$(4\pi,2\pi)$	(2.94, 0.95, 2.94)

approaches. This is representative of aquatic sediments and also similar to experimental domains of Voermans, Ghisalberti, and Ivey[10], Manes *et al.*[11] and numerical simulation domains of Fang *et al.*[35], Bomminayuni and Stoesser[36]. The length of the streamwise and spanwise domains is typical of turbulent, wall-bounded channel flows[37]. The grid resolutions for the PR-DNS study involved a highly refined mesh in the bed-normal direction in the top layer of the sediment bed resulting in about 90 grid points within each sediment particle. A systematic grid refinement study was also conducted and is reported in detail in Karra *et al.*[1] (see Appendix A). Finally, a baseline smooth wall case (SW) is also simulated in addition to the permeable bed cases to compare and contrast the influence of bed roughness and permeability on turbulence structure above the sediment bed. The bottom wall is defined as no slip boundary whereas a slip boundary condition is applied at the free surface. The wall normal grid resolution for the SW case is the same as PR-DNS case above the interface. The SW case uses DNS resolution, with the same streamwise and spanwise dimensions as the PR-DNS and VaNS-LES as given in Table I. For the VaNS-LES cases, the grid resolutions are finer in the spanwise and streamwise directions compared to typical open channel LES computations to ensure that the predictions are least affected by the grid resolution, but are a result of the diffuse porosity model used.

B. Variable porosity model

For the VaNS-LES approach, specification of a continuously varying porosity is needed. It is assumed that the porosity varies only in the bed-normal direction with a value of 1 in the freestream and $\varepsilon_\gamma = \varepsilon_c = 0.418$ in the homogeneous porous bed. The porosity

variation is directly obtained using the sediment bed generated in the PR-DNS study[1] as shown in figure 2b. Knowing the size of each particle and its centroid location, porosity field is obtained by applying the volume filtering defined in equation 1. For this, an appropriate choice of the filtering volume is needed.

For DNS or LES of the open-channel turbulent flow over a smooth wall, the grid normal to the wall is significantly refined so that the $y^+ = yu_\tau/\nu < 1$ near the wall to be within the viscous sublayer and capture the velocity gradient and shear stress accurately. The volume of the computational cell is then used as the filter width in the freestream. Similar grid refinement is necessary in the present simulation over a porous bed. However, as one approaches the interface and the porous bed region, a larger averaging volume is needed for the VaNS equations to obtain smooth variations in the flow variables and porosity. Changing the filtering volume in the interface region and within the bed requires modification of the spatial averaging theorem (equation 5) as the average of the gradient and gradient of the average do not commute and will result in additional terms due to variations in averaging volume[24,25]. To avoid large commutation errors in the interface region, a slowly varying averaging volume and grid resolution normal to the bed is used. Specifically, same bed-normal resolution as the resolution of the first grid point within the freestream is used for a region covering the entire top layer of the sediment bed. The grid is then gradually coarsened within the bed and the bed-normal grid resolution is given as,

$$
\begin{aligned}
&y = \ell_1 \eta_1 && \text{Region 1 (near bottom)} && -1.14 \leq y/\delta \leq -0.57 \\
&y = \frac{l_2 \tanh(\gamma_1 \eta_2)}{\tanh(\gamma_1)} && \text{Region 2 (homogeneous region)} && -0.57 < y/\delta \leq -0.28 \\
&y = \ell_3 \eta_3 && \text{Region 3 (top sediment layer)} && -0.28 < y/\delta \leq 0.031 \\
&y = \frac{\ell_4 \left(1 - \tanh(\gamma_2 - \gamma_2 \eta_3)\right)}{\tanh(\gamma_2)} && \text{Region 4 (freestream)} && 0.031 < y/\delta \leq 1,
\end{aligned}
$$

where ℓ_1, ℓ_2, ℓ_3, and ℓ_4 are the vertical heights of each region, γ_1 and γ_2 control the rate of transitioning of the averaging volume height in the bed-normal direction, $\eta_1 = \eta/w_1, \eta_2 = (\eta - w_1)/w_2, \eta_3 = (\eta - (w_1 + w_2))/w_3$, and $\eta = j/gnj$. Here, values w are weights based on the ratio of number of assigned volumes for averaging in each region and the total number of volumes, j is the index of the averaging volume, gnj is the total number of averaging volumes used in the bed normal direction. Typical γ_1 and γ_2 values are between $1.5 - 3$ and

$0.7 - 1.3$, respectively. Similar variable volume averaging was used in the PR-DNS Karra *et al.*[1].

Accordingly, a 'thin-volume' with filter width equal to the grid resolution in the bed-normal direction (ℓ_y) is assumed. For open-channel flows, variations normal to the wall are of interest and statistics are averaged in the homogeneous (wall parallel) directions. Accordingly, the filter lengths for the thin volume in the axial and spanwise directions are much larger, and proportional to the particle size. With this thin filter volume, the porosity variation is directly computed using the size and location of the sediment particles from the PR-DNS. The corresponding porosity variation in the bed-normal direction is shown

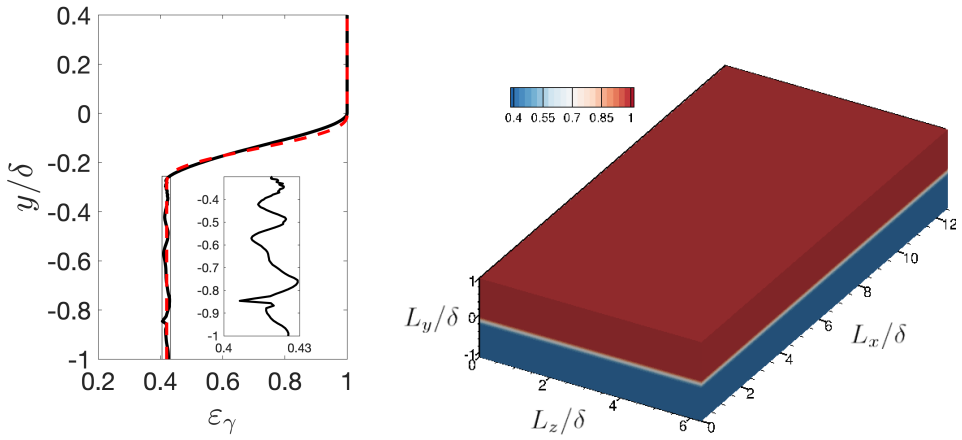

(a) Bed porosity (b) VaNS-LES

FIG. 3. Variable porosity model: (a) volume filtered porosity profile obtained directly from the sediment particle locations used in PR-DNS PR-DNS (—) case (inset shows small wiggles in the porosity within the bed), fifth order polynomial model fit (- -) case, and (b) porosity field specified in the VaNS-LES domain.

in figure 3a. Even with the thin-volume used to compute the bed-normal porosity, the local 'wiggles' within the bed are small (between 0.4–0.43) throughout the bed, even near the bottom of the domain. This is potentially because the interstitial gaps within the homogeneous region for a densely packed bed are small. Given that the porosity variations within the homogeneous region as obtained from the thin-volume averaging are small, a fifth order polynomial model fit to the porosity profile to remove any small wiggles is used. This polynomial model is similar to the one used by Breugem, Boersma, and Uittenbogaard[29]

and is given as

$$\varepsilon_\gamma(y) = -6(\varepsilon_c - 1)\left(\frac{y}{\delta_i}\right)^5 - 15(\varepsilon_c - 1)\left(\frac{y}{\delta_i}\right)^4 - 10(\varepsilon_c - 1)\left(\frac{y}{\delta_i}\right)^3 + 1. \tag{20}$$

For the present case, using $\delta_i = D_p$ results in a near perfect fit to the directly computed porosity variation. The corresponding porosity contours in the VaNS-LES domain are shown in figure 3b. With only bed-normal variation in the porosity, the homogeneous directions x and z is used for filtering.

Similar to the PR-DNS case, uniform grids are used in x and z directions for the VaNS-LES case. While coarser than the PR-DNS case, they are much finer than the typical resolutions used in LES studies smooth wall open channel flows. Importantly, the grid resolution in the bed-normal direction is exactly the same for both the LES and PR-DNS simulations in the the top layer of the sediment bed and extending slightly into the free-stream transition. This further results in small contribution of the subfilter scale stress in the present simulation and also minimizes the effect of grid resolution on predictions. Thus, any deviations in model predictions can be attributed to diffuse porosity model together with specification of the drag force in the interface region. The total grid count of about 33 million grid cells for the VaNS-LES is approximately seven times smaller than the PR-DNS case which results in significantly lower computational cost in terms of number of CPUs used and the total run time. With coarser mesh in the spanwise and streamwise directions, the VaNS-LES model will be much faster and applicable to larger, practical domain sizes.

C. Flow Setup

The flow in the simulations is driven by a body force imposed to obtain a constant target mass flow rate. The target mass flow rate is adjusted until the friction velocity, u_τ, which results in the required Re_K is obtained. Re_τ is then calculated based on the free-stream height, δ. The friction velocity, u_τ, is calculated from the maximum value of the time-space averaged total stress for the PR-DNS[1,34] and VaNS cases. It is important to note that the total shear stress is a sum of the viscous shear stress, $\rho\nu\partial(\langle\overline{u}\rangle)/\partial y$ and the Reynolds shear stress, $-\rho\langle\overline{u'v'}\rangle$. For PR-DNS, the form-induced shear stress, $-\rho\langle\widetilde{u}\widetilde{v}\rangle$, also contributes to the total shear stress. Following smooth wall DNS studies by Moser, Kim, and Mansour [37],

between 20-25 flow-through times (computed as the length over average bulk velocity L_x/U_b) are needed for the turbulent flow to reach stationary state. Once a stationary flow field is obtained, computations were performed for an additional time period of $T = 13\delta/u_\tau$ to collect single-point and two-points statistics. The non-dimensional time step sizes for the PR-DNS, VaNS-LES and SW cases are $9.30\times10^{-5}u_\tau/\delta$, $1.69\times10^{-4}u_\tau/\delta$, and $1.02\times10^{-4}u_\tau/\delta$.

IV. RESULTS

The main results for the different cases studied in this work are discussed. The VaNS-LES predictions are compared against the experimental and PR-DNS data for the verification and validation study (VV) first. Detailed qualitative and quantitative analysis of the instantaneous flow, space-time averaged statistics of the mean and Reynolds stresses, the turbulent kinetic energy budget, and the statistics of pressure fluctuations at the sediment crest are described next.

A. Validation Study

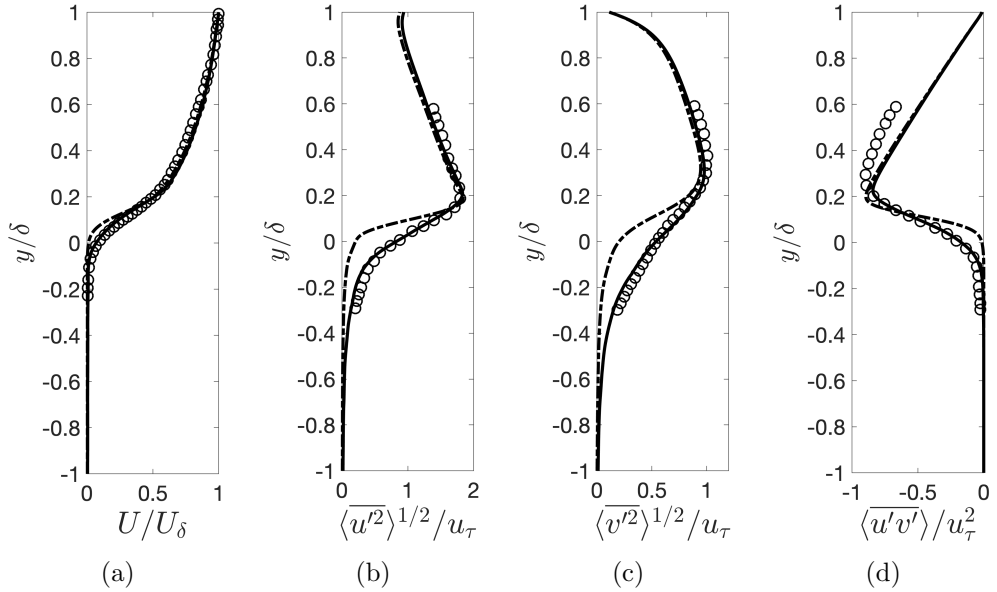

FIG. 4. Comparison of (a) mean streamwise velocity and (b) streamwise, (c) wall-normal, and (d) shear components of spatially averaged Reynolds stress tensor. Experimental data by Voermans, Ghisalberti, and Ivey[10] (○), VaNS-LES (-·-), PR-DNS from Karra *et al.*[1] (—).

VaNS-LES study of turbulent flow over a sediment bed is first compared with the ex-

perimental data of Voermans, Ghisalberti, and Ivey[10] (case L12 from their work) as well as the PR-DNS data of Karra *et al.*[1] (see Appendix C in Karra *et al.*[1] for more details). The time-space averaged mean velocity profile normalized by channel free-stream velocity, U_δ, is shown in figure 4a showing excellent agreement with the experimental and PR-DNS data. Voermans, Ghisalberti, and Ivey[10] defined the origin of the sediment bed to be the inflection point in the porosity profile, that is, where $\partial^2_{yy}\phi = 0$ (the inflection point). For these plots, in order to be able to compare with the experimental data, the origin for case VaNS-LES and PR-DNS are taken to be the inflection point of its porosity profile. It should be noted that the random packing obtained in the PR-DNS is different than that used in the experimental data; however, the bed porosity and the size of monodispersed particles is matched. The good agreement between the PR-DNS and the experimental data suggests that the actual location of the particles in a random arrangement is not significant for the present closed-packing. The actual locations of sphere centers can be important; however, if an arranged packing of spheres is considered.

Figures 4b, 4c, and 4d show a comparison of the normalized turbulence intensities, namely streamwise, bed-normal and shear stresses, respectively. The PR-DNS data matches well with the experiments within the bed as well as in the free stream for the streamwise and bed-normal intensities. The VaNS-LES prediction agrees with the experiments and PR-DNS in the free stream and deep inside the bed; however, underpredicts the intensities in the interface region. For the Reynolds shear stress, the PR-DNS predictions in the free stream deviate from the experimental data, but agree well within the bed. This is attributed to the high measurement uncertainty documented to be between $6 - 30\%$ Voermans, Ghisalberti, and Ivey[10] in sampling this variable in the experiment. The VaNS-LES model agrees with the PR-DNS data except in the interface region where the shear stress is again underpredicted. The underprediction of intensities in the interface transition region for the VaNS-LES model are attributed to the overestimation the drag force in this region of sharp variations in porosity and is discussed below in section IV B.

B. Mean flow and Reynolds stresses

Figure 5 shows the time-space averaged mean velocity and Reynolds stresses for the three cases (PR-DNS, VaNS-LES, and SW) at $Re_\tau \sim 270$. The variables are normalized by the

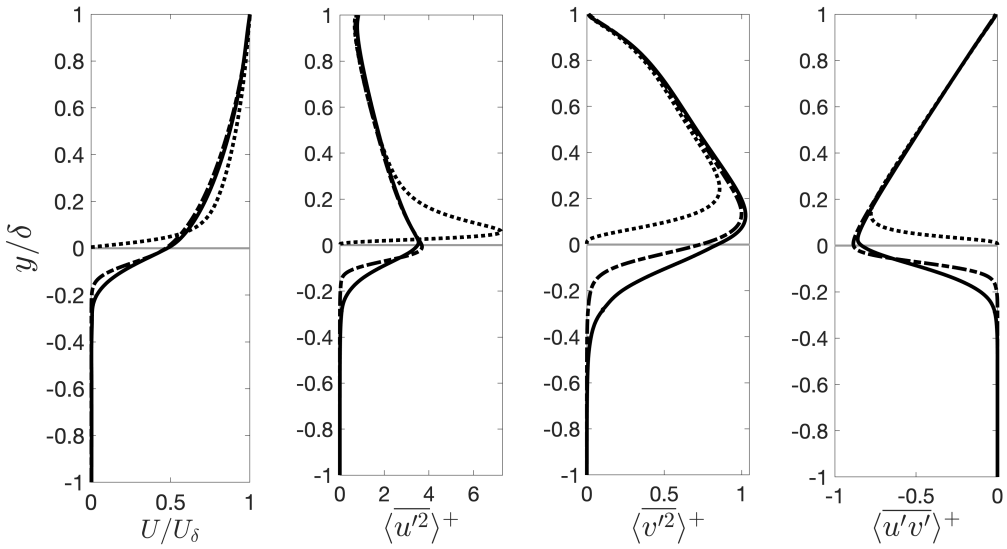

FIG. 5. Comparison of the mean velocity and turbulent stress profiles for VaNS-LES (-··-), PR-DNS (—), and SW (···) cases: (a) mean velocity and (b-d) streamwise, wall-normal, and shear components of Reynolds stress tensor. Horizontal line (—) shows the crest of sediment bed for PR-DNS and VaNS-LES cases and the underlying no-slip wall for the SW case.

friction velocity, u_τ (mean velocity by U_δ), and y is normalized by free-stream height, δ. Here, $y = 0$ corresponds to the sediment crest. The profiles of mean velocity, and Reynolds stresses for the PR-DNS and VaNS-LES cases compare reasonably well with each other. Some differences are observed near the sediment crest and within the transition region. This is attributed to (i) roughness effects present in PR-DNS in a randomly-packed bed, but absent in the VaNS-LES, and (ii) overprediction of the drag force in the interface region based on the standard permeability model. In PR-DNS of the randomly-packed sediment bed, the top layer consists of particles that protrude into the freestream and are relatively exposed compared to the sediment particles within the bed. Since the porosity variation used in the present VaNS-LES is uniform in the x-z plane, such roughness effect is absent in the VaNS-LES configuration. The roughness elements cause a slightly greater mean velocity deficit in the PR-DNS case. Compared to the smooth wall case though, both the permeable bed cases show a mean velocity deficit due to bed permeability and roughness caused momentum loss.

In the VaNS-LES case, the streamwise Reynolds stress, $\langle\overline{u'^2}\rangle^+$, shows slightly greater tangential spread near the crest whereas the bed-normal Reynolds stress, $\langle\overline{v'^2}\rangle$ penetration below the crest is lower compared to PR-DNS. The random spread of the roughness pro-

trusions in the top layer creates distinct channels through which flow can penetrate under the particles resulting in slightly greater loss in streamwise stress intensity and deeper bed-normal stress penetration. In other words, even though the average porosity for the PR-DNS and VaNS-LES cases is the same, the local porosity variations in the PR-DNS case create an uneven wall-blocking effect compared to VaNS-LES which has a uniform wall-blocking effect. This can be observed from the gradient of change for the stresses from their peak locations near the crest into the bed. The peaks in $\langle\overline{u'^2}\rangle$ (figure 5b) for the PR-DNS case happen slightly above the crest and the slope of change of the stress value is steeper, whereas for the VaNS-LES case the peak happens below the crest and the slope of change is shallower. Similar slope behavior can also be observed in $\langle\overline{v'^2}\rangle$ (figure 5c). For the smooth wall case, turbulent flow fluctuations toward the wall (i.e., sweeps) are redirected into wall parallel components due to the wall blocking effect resulting in greater tangential spread of the streamwise stress and lower peak in wall-normal stress away from the solid wall in the free stream. The Reynolds stress $\langle\overline{u'v'}\rangle^+$ (figure 5d) is higher for the permeable bed cases compared to the smooth wall indicating that bed permeability and roughness enhance shear stress. Similar behavior in peak value locations and slope of change of stress below the crest is observed in the shear stress between the two permeable bed cases.

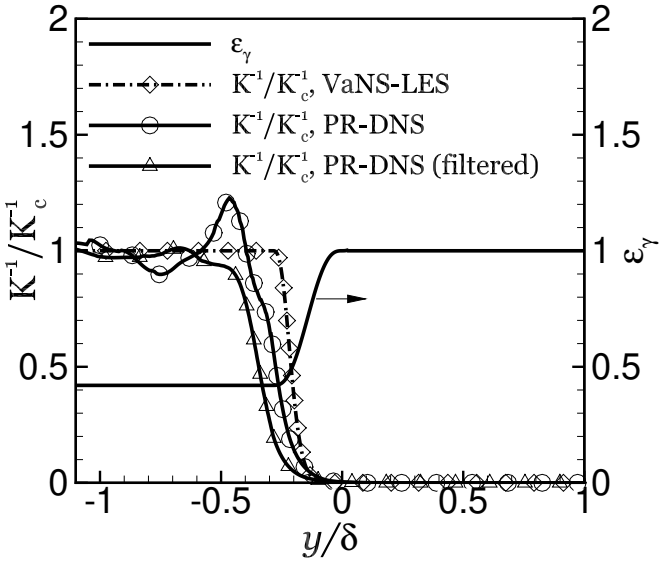

FIG. 6. Bed-normal variation of porosity and permeability normalized by its value deep within the bed: (-·-) VaNS-LES and PR-DNS (—). (The arrow points to the scale for ε_γ, which is the secondary y-axis on the right.)

To further understand the effect of the effective permeability model and drag force in the VaNS-LES model, the bed-normal variation of the effective inverse permeability ($\mathbf{K}^{-1}$) normalized by its value deep inside the bed ($\mathbf{K}_c{}^{-1}$) is plotted in figure 6 together with the bed-normal variation of porosity. Using the model for the permeability (equation 17 and equation 16), the normalized permeability is zero in the free-stream, varies in the region of porosity gradient, and approaches a value of 1 within the bed. Also plotted is value of the effective permeability obtained from the PR-DNS data using equation 15. Here, the drag force on the surface of the spheres from the PR-DNS calculation is directly integrated to obtain the effective permeability and then averaged in the homogeneous (x-z) planes. The effective permeability from PR-DNS also goes to zero within the freestream varies in the interface region and approaches unity within the bed. The PR-DNS permeability shows some fluctuations which is because of the randomness in the sphere locations. These fluctuations are more pronounced than those in the porosity field because the effective permeability is obtained by division of the intrinsic velocity which can become very small quickly away from the interface. If the permeability is filtered over a thickness of the size of the particle, the filtered permeability is much smoother as seen from figure 6. It is seen from these variations that the inverse of effective permeability obtained from PR-DNS is *smaller* in the interface region than that predicted by equation 16 in the interface region for PR-DNS. This indicates that the effective permeability value used within the VaNS-LES model is much lower in the interface region (or K^{-1} is larger) than that seen in the PR-DNS. This may in part help explain the underprediction of the bed-normal velocity fluctuations ($\langle\overline{v'^2}\rangle$) in the VaNS-LES model compared to PR-DNS. The permeability model (equation 17) used is designed for uniform porosity regions (such as deep within the bed), but not for variable porosity region. Figure 6 shows that the normalized inverse permeability predicted by the model matches well with that obtained from the filtered PR-DNS data, however, deviates in the region of sharp changes in porosity. Thus a modification of the drag closure in the interface region should be developed, and will be part of the future work.

C. Turbulence structure

Distinct variations in the characteristics of primary turbulence structure are first shown in this section followed by analysis of contribution to fluid shear stress on the sediment

bed. Contours of instantaneous bed-normal vorticity, $\omega_y^+ = \omega_y \nu / u_\tau^2$, are plotted at y=$0.005\delta$ (figure 7.), which is the location of maximum shear stress for VaNS-LES. This location is chosen so as to allow for a qualitative comparison of turbulence structures between the permeable bed and the smooth wall close to the crest of the bed. In the smooth wall case, distinct long elongated streaky structures, which are a result of low and high speed streaks generated quasi-streamwise vortices, are visible. The influence of strong mean velocity gradient and an impenetrable smooth wall results in these long streaky structures[38]. For the permeable bed, the breakdown of these structures is observed in both the PR-DNS and VaNS-LES. The roughness and permeability of the bed helps in the breakdown. Although the long elongated streaks are shortened due to roughness and permeability, at this Re_K the flow anisotropy is somewhat retained. Compared to the VaNS-LES case a wider range of spatial-scales of flow structures are visible in the PR-DNS case. The random distribution of roughness protrusions creates obstructions around and over which the turbulent flow mixing is more pronounced which leads to a greater spatial scale distribution in the PR-DNS.

Figure 8 shows contours of instantaneous bed-normal velocity. Weakening of wall blocking effect due to bed permeability results in turbulent flow penetrating into the sediment bed in both VaNS-LES and PR-DNS cases. Regions of positive and negative bed-normal velocity values, in permeable bed cases, are associated with sweeps and ejections of fluid parcels which carry both momentum and mass in and out of the bed. The contours for the VaNS case are more diffused near the bed whereas in the pore-resolved case flow structures are broken down and distributed (or influenced) by the roughness element protrusions.

Figure 9a,b shows the profiles for total fluid shear stress and the individual components comprising the total shear stress normalized by u_τ^2. The total shear stress profiles for both the permeable bed cases peak near the sediment bed crest and then decay quickly inside the bed (figure 9a) and show linear variation in the freestream. The peak value of the pore-resolved DNS is slightly larger than the VaNS case. The individual components for the fluid shear stress acting on the sediment are shown in figure 9b. For both the cases, the contribution from the Reynolds shear stress is the largest and the peak value occurs very close to the crest of the sediment bed. The contribution of bed permeability and roughness enhancing the turbulent shear stress can be clearly confirmed by this result. The viscous stress magnitude though lower than Reynolds stress is not negligible at the Re_K value studied in this work. Importantly, form-induced stress contribution to the pore-resolved DNS is larger than the

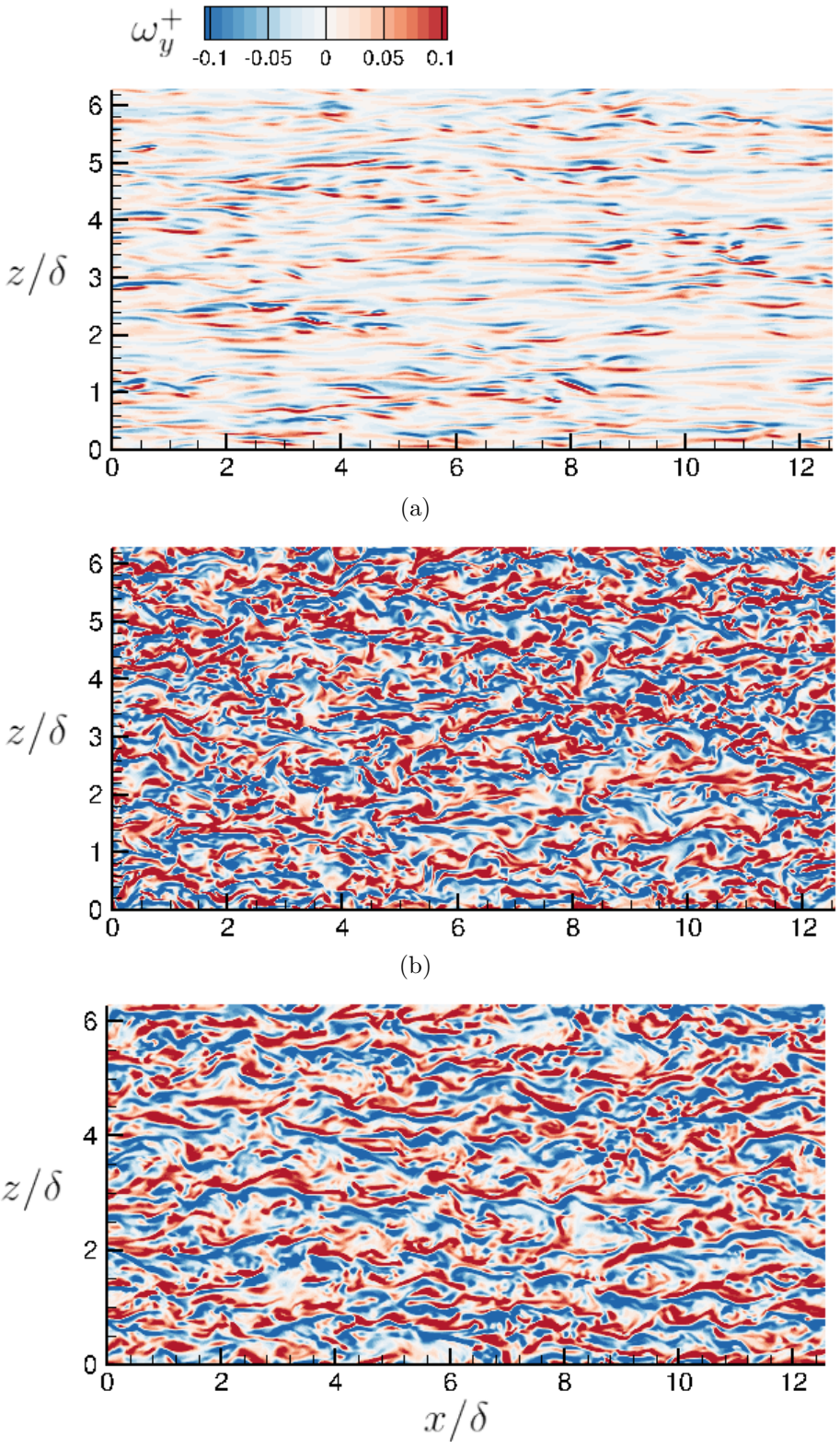

FIG. 7. Contours of bed-normal vorticity, ω_y^+, normalized by u_τ^2/ν at $y/\delta = 0.005$, for (a) SW, (b) PR-DNS and (c) VaNS-LES cases.

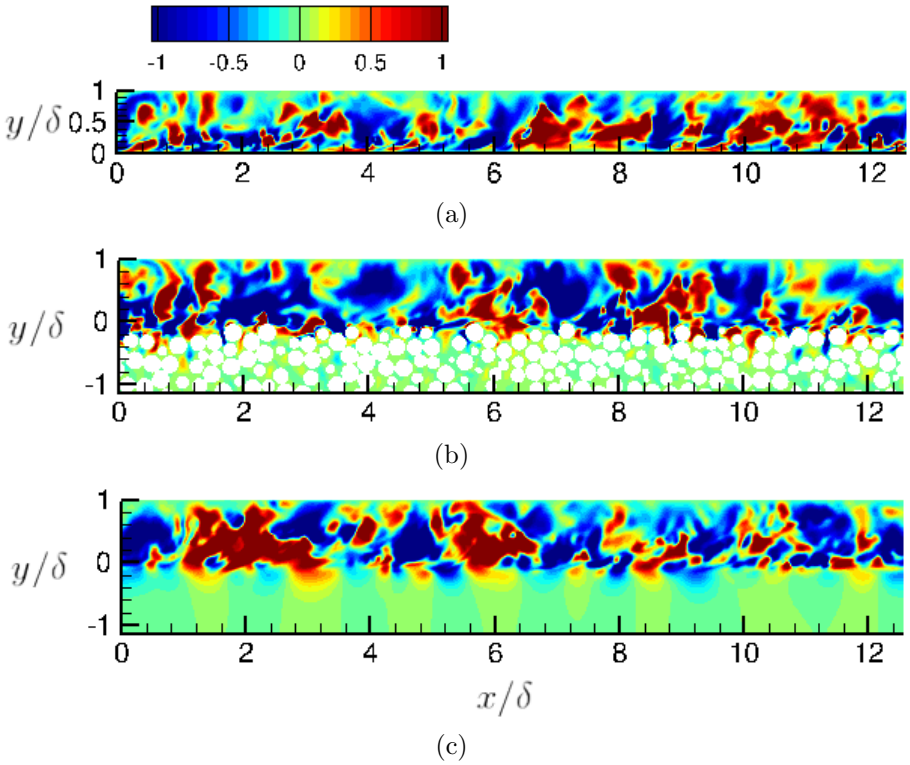

FIG. 8. Contours of bed-normal velocity for (a) SW (b) PR-DNS and (b) VaNS-LES cases shown on the z-normal symmetry plane.

viscous stress contribution. This is a direct contribution of the roughness protrusions, which are absent in the VaNS case, in enhancing the shear stress near the sediment bed which results in a more rigorous transport of fluid momentum in and out of the bed. The addition of the form-induced stress in the PR-DNS case results in larger magnitude of the total stress for that case.

The skin friction coefficient for wall bounded turbulent channel flows is defined as $C_f = 2(u_\tau/U_b)^2$ (where U_b = bulk velocity). The mean values of C_f for VaNS-LES, PR-DNS and SW cases are 1.82e-2, 1.83e-2, and 7.3e-3, respectively. The mean C_f value for the permeable bed cases is about 2.5 times that of the SW case and is associated with penetration of turbulence shear into the bed thereby increasing flow resistance as observed in figure 9.

D. TKE Budget

The TKE budget for both PR-DNS and VaNS-LES cases is analyzed to understand the role of different terms in energy production, transport, and dissipation. Following the

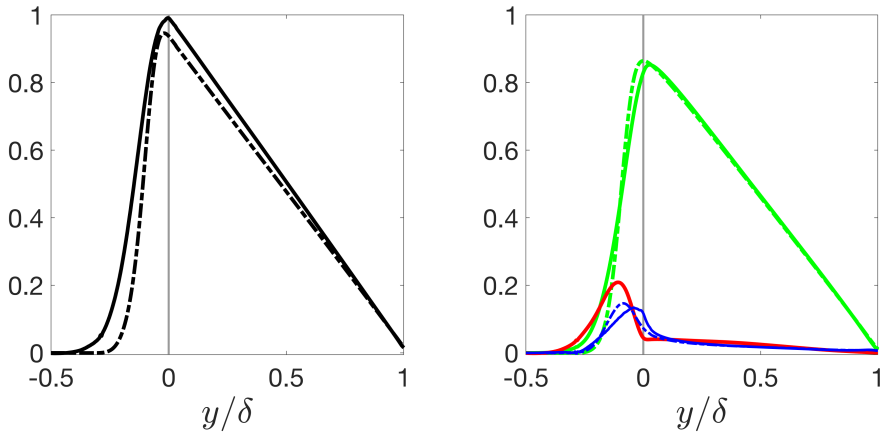

FIG. 9. Fluid shear stress profiles for the VaNS-LES (dash-dot lines) and PR-DNS (solid lines) cases. (a) Total fluid stress for the VaNS-DNS (-·-) and the PR-DNS (—) cases. The total shear stress is a sum of the viscous and Reynolds shear stress for the VaNS-LES case. The PR-DNS case in addition to these two stresses also has contribution from the form-induced stress. and (b) Reynolds stress ($-\rho\langle\overline{u'v'}\rangle$) for the VaNS-LES (-·-) and PR-DNS (—) cases; Viscous stress ($\rho\nu\partial(\langle\overline{u}\rangle)/\partial y$) for the VaNS-LES (-·-) and the PR-DNS (—) cases ; Form-induced stress ($-\rho\langle\widetilde{u}\widetilde{v}\rangle$) for the PR-DNS (—) case.

literature on flow over macro-roughness beds[39] and canopies[40,41] the equations become,

$$\frac{\partial\langle\overline{u_i'u_i'}\rangle/2}{\partial t} = \underbrace{-\langle\overline{u_i'v'}\rangle\frac{\partial\langle\overline{u_i}\rangle}{\partial y}}_{P_s} + \left[\underbrace{-\left\langle\widetilde{u_i'u_j'}\frac{\partial\tilde{u}_i}{\partial x_j}\right\rangle}_{P_w} \underbrace{-\langle\overline{u_i'u_j'}\rangle\left\langle\frac{\partial\tilde{u}_i}{\partial x_j}\right\rangle}_{P_m}\right] - \frac{\partial}{\partial y}\left[\underbrace{\langle\overline{u_i'u_i'v'}\rangle/2}_{T_t} + \underbrace{\langle\widetilde{u_i'u_i'}\tilde{v}\rangle/2}_{T_w}\right] \underbrace{-\frac{1}{\rho}\frac{\partial}{\partial y}\langle\overline{p'v'}\rangle}_{T_p} \underbrace{+\nu\frac{\partial^2}{\partial y^2}\langle\overline{u_i'u_i'}\rangle/2}_{T_\nu} - \langle\bar{\epsilon}\rangle. \quad (21)$$

The eight terms on the right hand side of the equation 21 are defined as follows: the shear production term, P_s, represents the work of the time-space averaged velocity against the time-space averaged shear; the wake production term, P_w, is the work of wake-induced velocity disturbances against the bed-induced shear; form induced production, P_m, is the work of the bed-induced velocity fluctuations against time-space averaged shear; $\partial T_t/\partial y$, is turbulent transport; $\partial T_w/\partial y$, is the bed-induced turbulent transport; T_p is pressure transport; T_ν is viscous transport of TKE and the last term on the right represents viscous dissipation, ϵ. Here the terms P_m, P_w and T_w arise as a result of spatial heterogeneity at

the roughness element length scale and hence are only relevant to the PR-DNS case.

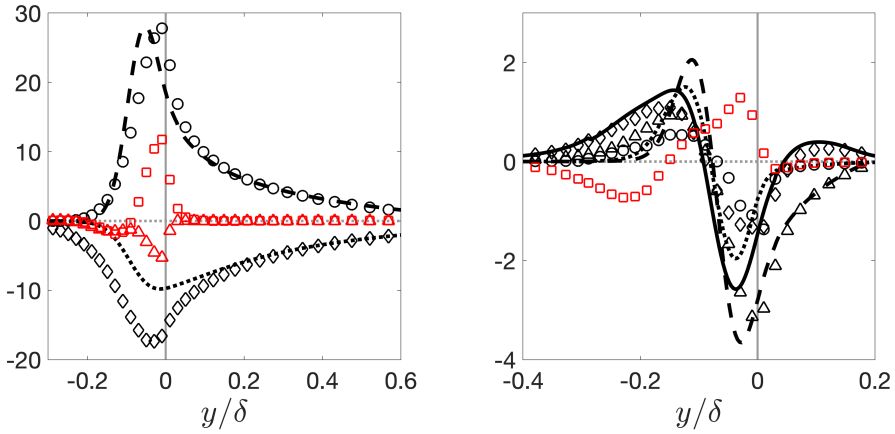

FIG. 10. (a) Bed-normal variation of TKE production and dissipation terms for VaNS-LES (lines) and PR-DNS cases (symbols); Legend: (P_s, - -, ○), (P_m, □), (P_w, △), (ϵ, ···, ◇), (b) Bed-normal variation of TKE transport terms for VaNS-LES (lines) and PR-DNS cases (symbols); Legend: (T_t, - -, △), (T_w, □), (T_ν, ···, ○), (T_p, —, ◇). Vertical line shows the bed crest (—).

Figure 10a shows the variation of the production, dissipation terms. Shear production, P_s, in both the permeable bed cases peaks below the crest, with the peak for PR-DNS case deeper in the bed consistent with other turbulent statistics discussed so far. The additional wake production terms P_m, P_w (figure 10a) for the pore-resolved case also peak below the crest. Both P_m and P_w are comparable in magnitude to the shear production term, P_s. Negative peak in P_w at the roughness crest level is observed and could be attributed to the conversion of turbulent kinetic energy to wake kinetic energy as a result of work of large-scale structures (greater than roughness scale) associated with $\langle\overline{u'^2}\rangle^+$ at this location acting against the pressure drag of roughness elements. The peak value for dissipation, ϵ is at a similar location as the shear production for both cases. However, the magnitude of dissipation for the PR-DNS case is greater than the VaNS-LES case as the additional wake production terms also need to be dissipated. Further away from the sediment crest, for $y/\delta > 0.5$, the shear production P_s and dissipation ϵ reach an equilibrium where the rate of production balances the rate of dissipation.

Figure 10b shows the transport terms. In both the cases the turbulent transport, T_t, and pressure transport, T_p, are of comparable magnitude near the crest region and work in transporting the high TKE, produced here, primarily into the bed and some of it into

the near bed free-stream region. The viscous transport, T_ν, though small is not negligible and moves energy from high TKE region to low TKE region. For the PR-DNS case the form induced transport, T_w, is significant and works against the other transport processes by moving the TKE upwards from a low-TKE region inside the bed to the crest region.

E. Turbulent pressure fluctuations

Pressure fluctuations at the sediment-water interface play a critical role in mass and momentum transport in and out of the sediment bed. Specifically, pressure fluctuations due to turbulence are conjectured to have significant impact on mass transport within the hyporheic zone as it can directly influence the residence times through turbulent advection. Normalized mean square pressure fluctuation statistics for all three cases are compared in figure 11. The pressure fluctuation magnitudes are larger for both the permeable beds com-

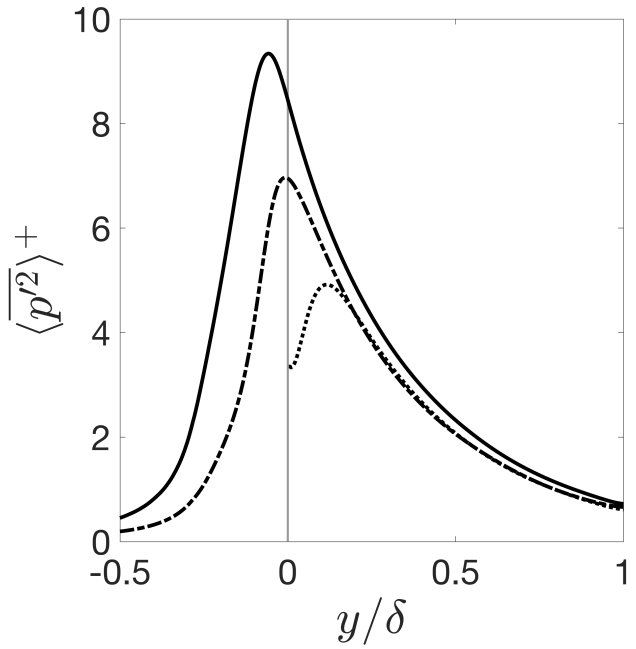

FIG. 11. Profiles of mean-square pressure fluctuations $\langle\overline{p'^2}\rangle^+$ for VaNS-LES (-·-), PR-DNS (—), and SW (···) cases. Pressure is normalized by ρu_τ^2. Vertical line shows the crest of sediment bed (—).

pared to the smooth wall case. The peak value of the pressure fluctuations for the smooth wall case is observed at $y^+ \sim 30$. The peak for VaNS-LES case is closer to the crest (slightly below it), while for the PR-DNS case it is further away from the crest. The fluctuations

quickly decay for $y/\delta < -0.5$, indicating that majority of the pressure fluctuations of significant magnitude are restricted to the top layer of the sediment bed. Importantly, the peak value predicted by the VaNS case is lower than the pore-resolved case, clearly showing that turbulence fluctuations are enhanced in the PR-DNS which can in part be attributed to the influence of roughness protrusions as well as higher effective permeability (lower $\mathbf{K}^{-1}$) observed in the PR-DNS as compared to the VaNS-LES model. To better capture the influence of roughness protrusions in the VaNS-LES model, the current approach of using a porosity varying only in the bed-normal direction should be modified. Using a filter kernel that varies proportional to the particle size, a porosity field that varies in the spanwise and streamwise directions in addition to the bed-normal variation can be obtained. Designing such an appropriate filter kernel that does not give rise to strong oscillations in drag force is necessary and will be part of the future work.

V. CONCLUSIONS

Numerical investigation of a turbulent boundary layer over a porous sediment bed at permeability Reynolds number of $Re_k \sim 2.56$ (Re_τ=270) representative of aquatic systems is performed using a continuum approach based on the volume-averaged Navier-Stokes (VaNS) equations developed by defining a smoothly varying porosity across the bed interface. The porosity profile is obtained by matching it to the averaged porosity from a randomly distributed, monodispersed sediment particles bed used in the pore-resolved DNS[1]. The drag force in the porous bed was modeled using a modified Ergun equation with Forchheimer corrections for inertial terms[27,29]. The time-space averaging methodology is used to compute the mean velocity and Reynolds stresses. Differences in the near-bed turbulence structure, fluid shear stress acting on sediment bed, turbulent pressure fluctuations and TKE budget were quantified in detail. The key findings of this work are summarized below.

(i) Mean velocity and Reynolds stresses generally compare well for the VaNS and pore-resolved DNS cases. Small differences observed near the sediment bed crest are attributed to effect of roughness protrusions on the flow, which are absent in the VaNS-LES configuration. In addition, this randomness in the top layer results in higher effective permeability in the interface region in PR-DNS study, which creates spatially varying wall-blocking effect as compared to the VaNS-LES model which has nearly uniform wall-blocking effect, resulting

in the differences observed in the interface region. The standard Ergun-like model for the effective permeability, that is developed based on uniform porosity, predicts lower values (higher $\mathbf{K}^{-1}$) in the interface region and thus corrections to the model should be devised in regions of sharp variations in porosity.

(ii) The bed-normal vorticity contours in wall-units show that the long elongated streaks, a characteristic of flow over a smooth impermeable, are shortened due to roughness and permeability in both the permeable bed cases. Compared to VaNS-LES, a wider range of spatial-scales of flow structures are visible in the PR-DNS as it fully resolves the roughness protrusions. These roughness elements break down the flow structures resulting in much finer wider scales . Similarly, bed-normal instantaneous velocity contours appear more diffused near the sediment bed for the VaNS model; however, the overall flow field is similar to the PR-DNS result.

(iii) The total fluid stress in the permeable bed peaks just underneath the crest and then decays quickly inside the bed and is well captured by the VaNS-LES model. While the Reynolds shear stress contributes the most to the total fluid stress, the viscous shear stress is not negligible for the Re_K studied in this work. Importantly, form-induced stress contribution to the pore-resolved DNS is larger than the viscous stress contribution and results in the larger total stress.

(iv) The shear production in both VaNS and pore-resolved DNS is similar, though the pore-resolved case has additional contribution from wake induced production. In both cases, the turbulent and pressure transport are of comparable magnitude near the crest region and are responsible in transporting the high TKE, produced here, primarily into the bed and some of it into the near bed free-stream region. In PR-DNS, the form induced transport is significant and works against the other transport processes by moving the TKE upwards from a low-TKE region inside the bed to the crest region.

(v) The roughness protrusions present in the PR-DNS enhance the turbulent pressure fluctuations resulting in a higher peak value compared to the VaNS-LES case, which does not model these protrusions. The fluctuations quickly decay for $y/\delta < -0.5$, indicating that majority of the pressure fluctuations of significant magnitude are restricted to the top layer of the sediment bed.

The above findings show that an upscaled, continuum approach, based on volume-averaged Navier-Stokes equations, is capable of accurately predicting various primary and

secondary statistics for turbulent flow over flat sediment bed, in comparison to a high fidelity pore-resolved DNS simulation. Streamwise and spanwise variations in porosity at the SWI, representative of the particle protrusions in the top sediment layer, may further improve the predictions from the VaNS-LES, and should be investigated in the future. In addition, directly computing the bed-normal variations in effective permeability from the PR-DNS data may facilitate development of corrections to the permeability model in the regions of sharp gradients in porosity. The VaNS formulation can then be effectively used to solve mass and momentum exchange problem for flows over sediment beds at much higher permeability Reynolds numbers for flat as well as complex bedforms, which will be the focus of future studies.

ACKNOWLEDGMENTS

SVA acknowledges partial funding from US NSF (Award #205324) as well as US Department of Energy's Office of Basic Energy Sciences (Geosciences) DE-SC0021626. All computations were performed on Frontera computing resources under NSF's Leadership Resources Allocation (LRAC).

REFERENCES

[1]S. K. Karra, S. V. Apte, X. He, and T. D. Scheibe, "Pore-resolved investigation of turbulent open channel flow over a randomly packed permeable sediment bed," Journal of Fluid Mechanics **971**, A23 (2023).

[2]K. Bencala, R. Rathbun, A. P. Jackman, V. Kennedy, G. Zellweger, and R. Avanzino, "Rhodamine wt dye losses in a mountain stream environment," Water Resources Bulletin **19**, 943–950 (1983).

[3]D. D'angelo, J. Webster, S. Gregory, and J. Meyer, "Transient storage in appalachian and cascade mountain streams as related to hydraulic characteristics," Journal of the North American Benthological Society , 223–235 (1993).

[4]H. M. Valett, J. A. Morrice, C. N. Dahm, and M. E. Campana, "Parent lithology, surface–groundwater exchange, and nitrate retention in headwater streams," Limnology and oceanography **41**, 333–345 (1996).

[5]J. W. Harvey, B. J. Wagner, and K. E. Bencala, "Evaluating the reliability of the stream tracer approach to characterize stream-subsurface water exchange," Water Resources Research **32**, 2441–2451 (1996).

[6]M. P. Anderson *et al.*, *Groundwater: Selection, Introduction and Commentary.* (IAHS Press, 2008).

[7]M. A. Briggs, M. N. Gooseff, C. D. Arp, and M. A. Baker, "A method for estimating surface transient storage parameters for streams with concurrent hyporheic storage," Water Resources Research **45** (2009).

[8]S. B. Grant, J. D. Gomez-Velez, and M. Ghisalberti, "Modeling the effects of turbulence on hyporheic exchange and local-to-global nutrient processing in streams," Water Resources Research **54**, 5883–5889 (2018).

[9]E. T. Hester, M. B. Cardenas, R. Haggerty, and S. V. Apte, "The importance and challenge of hyporheic mixing," Water Resources Research **53**, 3565–3575 (2017).

[10]J. Voermans, M. Ghisalberti, and G. Ivey, "The variation of flow and turbulence across the sediment–water interface," Journal of Fluid Mechanics **824**, 413–437 (2017).

[11]C. Manes, D. Pokrajac, I. McEwan, and V. Nikora, "Turbulence structure of open channel flows over permeable and impermeable beds: A comparative study," Physics of Fluids **21**, 125109 (2009).

[12]T. Kim, G. Blois, J. L. Best, and K. T. Christensen, "Experimental evidence of amplitude modulation in permeable-wall turbulence," Journal of Fluid Mechanics **887** (2020).

[13]S. Whitaker, "The forchheimer equation: a theoretical development," Transport in Porous media **25**, 27–61 (1996).

[14]J. A. Ochoa-Tapia and S. Whitaker, "Momentum transfer at the boundary between a porous medium and a homogeneous fluid—i. theoretical development," International Journal of Heat and Mass Transfer **38**, 2635–2646 (1995).

[15]J. A. Ochoa-Tapia and S. Whitaker, "Momentum transfer at the boundary between a porous medium and a homogeneous fluid—ii. comparison with experiment," International Journal of Heat and Mass Transfer **38**, 2647–2655 (1995).

[16]M. E. Rosti, L. Cortelezzi, and M. Quadrio, "Direct numerical simulation of turbulent channel flow over porous walls," Journal of Fluid Mechanics **784**, 396–442 (2015).

[17]G. S. Beavers and D. D. Joseph, "Boundary conditions at a naturally permeable wall," Journal of fluid mechanics **30**, 197–207 (1967).

[18]P. G. Saffman, "On the boundary condition at the surface of a porous medium," Studies in applied mathematics **50**, 93–101 (1971).

[19]S. Hahn, J. Je, and H. Choi, "Direct numerical simulation of turbulent channel flow with permeable walls," Journal of Fluid Mechanics **450**, 259–285 (2002).

[20]B. Goyeau, D. Lhuillier, D. Gobin, and M. Velarde, "Momentum transport at a fluid–porous interface," International Journal of Heat and Mass Transfer **46**, 4071–4081 (2003).

[21]U. Shavit, G. Bar-Yosef, R. Rosenzweig, and S. Assouline, "Modified brinkman equation for a free flow problem at the interface of porous surfaces: The cantor-taylor brush configuration case," Water resources research **38**, 56–1 (2002).

[22]T. Duman and U. Shavit, "A solution of the laminar flow for a gradual transition between porous and fluid domains," Water Resources Research **46** (2010).

[23]W.-P. Breugem and B.-J. Boersma, "Direct numerical simulations of turbulent flow over a permeable wall using a direct and a continuum approach," Physics of fluids **17**, 025103 (2005).

[24]D. Pokrajac and M. De Lemos, "Spatial averaging over a variable volume and its application to boundary-layer flows over permeable walls," Journal of Hydraulic Engineering **141**, 04014087 (2015).

[25]W. Sadowski, M. Sayyari, F. Di Mare, and H. Marschall, "Large eddy simulation of flow in porous media: Analysis of the commutation error of the double-averaged equations," Physics of Fluids **35** (2023).

[26]M. Quintard and S. Whitaker, "Convection, dispersion, and interfacial transport of contaminants: Homogeneous porous media," Advances in Water resources **17**, 221–239 (1994).

[27]B. D. Wood, X. He, and S. V. Apte, "Modeling turbulent flows in porous media," Annual Review of Fluid Mechanics **52**, 171–203 (2020).

[28]M. Germano, U. Piomelli, P. Moin, and W. H. Cabot, "A dynamic subgrid-scale eddy viscosity model," Physics of Fluids A: Fluid Dynamics **3**, 1760–1765 (1991).

[29]W. Breugem, B. Boersma, and R. Uittenbogaard, "The influence of wall permeability on turbulent channel flow," Journal of Fluid Mechanics **562**, 35 (2006).

[30]R. Bird, W. Stewart, and E. Lightfoot, "Transport phenomena. john wiley & sons, inc," New York, NY **1** (2002).

[31]I. Macdonald, M. El-Sayed, K. Mow, and F. Dullien, "Flow through porous media-the ergun equation revisited," Industrial & Engineering Chemistry Fundamentals **18**, 199–208

(1979).

[32]Ö. Bağcı, N. Dukhan, and M. Özdemir, "Flow regimes in packed beds of spheres from pre-darcy to turbulent," Transport in porous media **104**, 501–520 (2014).

[33]A. M. Wilson, M. Huettel, and S. Klein, "Grain size and depositional environment as predictors of permeability in coastal marine sands," Estuarine, Coastal and Shelf Science **80**, 193–199 (2008).

[34]S. K. Karra, X. He, S. Apte, and T. D. Scheibe, "Particle resolved dns study of turbulence effects on hyporheic mixing in randomly packed sediment beds," in *Proceedings Of TSFP-12 (2022) Osaka* (2022).

[35]H. Fang, H. Xu, G. He, and S. Dey, "Influence of permeable beds on hydraulically macro-rough flow," Journal of Fluid Mechanics **847**, 552–590 (2018).

[36]S. Bomminayuni and T. Stoesser, "Turbulence statistics in an open-channel flow over a rough bed," Journal of Hydraulic Engineering **137**, 1347–1358 (2011).

[37]R. D. Moser, J. Kim, and N. N. Mansour, "Direct numerical simulation of turbulent channel flow up to re τ= 590," Physics of fluids **11**, 943–945 (1999).

[38]M. J. Lee, J. Kim, and P. Moin, "Structure of turbulence at high shear rate," Journal of Fluid Mechanics **216**, 561–583 (1990).

[39]E. Mignot, E. Barthélemy, and D. Hurther, "Double-averaging analysis and local flow characterization of near-bed turbulence in gravel-bed channel flows," Journal of Fluid Mechanics **618**, 279–303 (2009).

[40]M. R. Raupach and R. Shaw, "Averaging procedures for flow within vegetation canopies," Boundary-Layer Meteorology **22**, 79–90 (1982).

[41]M. Raupach and A. S. Thom, "Turbulence in and above plant canopies," Annual Review of Fluid Mechanics **13**, 97–129 (1981).